Cell Reports
Physical Science

CellPress
OPEN ACCESS

Article

Direct visualization of electrochemical reactions and heterogeneous transport within porous electrodes *in operando* by fluorescence microscopy

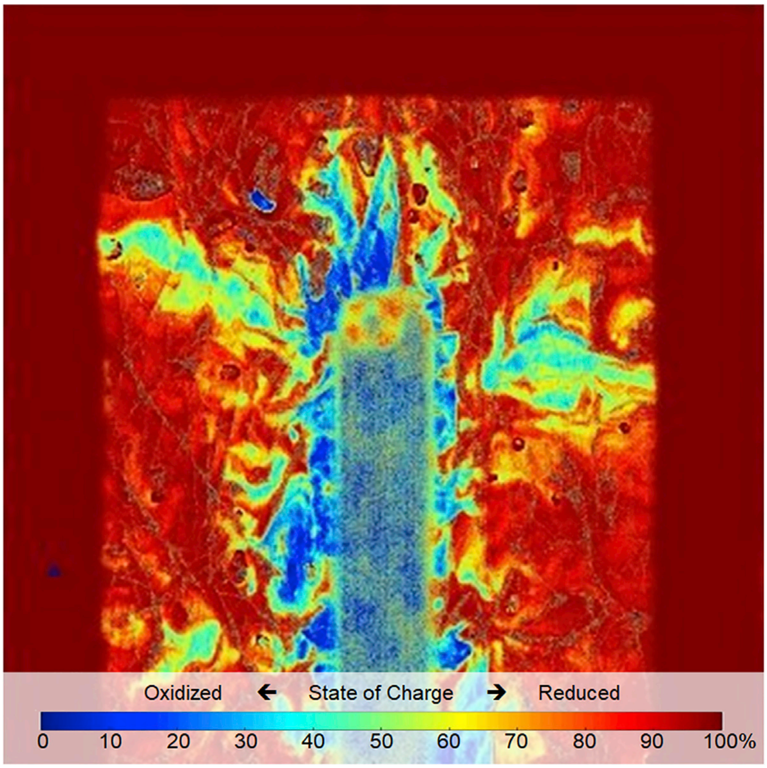

Wong et al. demonstrate the use of electrochemical fluorescence microscopy applied to redox-active, fluorescent quinones for high spatial-temporal reaction-flow mapping *operando* within porous electrodes. Surprising heterogeneous mass transport behavior was observed within electrode materials common to flow battery and fuel cells.

Video in supplemental information at https://www.sciencedirect.com/science/article/pii/S2666386421000783#mmc2

Andrew A. Wong, Shmuel M. Rubinstein, Michael J. Aziz

maziz@harvard.edu

HIGHLIGHTS

Operando electrolyte reaction-flow mapping within porous electrodes

Quantified local state of charge with micron- and sub-second resolution

2D particle tracing measuring spatial flow profiles within tortuous structures

Coupled electrochemical concentration polarization with spatial state of charge maps

Wong et al., Cell Reports Physical Science *2*, 100388
April 21, 2021
https://doi.org/10.1016/j.xcrp.2021.100388

Please cite this article in press as: Wong et al., Direct visualization of electrochemical reactions and heterogeneous transport within porous electrodes *in operando* by fluorescence microscopy, Cell Reports Physical Science (2021), https://doi.org/10.1016/j.xcrp.2021.100388

Cell Reports
Physical Science

CellPress
OPEN ACCESS

Article

Direct visualization of electrochemical reactions and heterogeneous transport within porous electrodes *in operando* by fluorescence microscopy

Andrew A. Wong,[1,2] Shmuel M. Rubinstein,[1,3] and Michael J. Aziz[1,4,*]

SUMMARY

Optical fluorescence microscopy is shown to enable both high spatial and temporal resolution of redox-dependent fluorescence in flowing electrolytes. We report the use of fluorescence microscopy coupled with electrochemistry to directly observe the reaction and transport of redox-active quinones within porous carbon electrodes *in operando*. We observe surprising electrolyte channeling features within several porous electrodes, leading to spatially distinguishable advection-dominated and diffusion-dominated regions. These results challenge the common assumption that transport in porous electrodes can be approximated by a homogeneous Darcy-like permeability, particularly at the length scales relevant to many electrochemical systems such as redox flow batteries. This work presents a new platform to provide highly resolved spatial and temporal insight into electrolyte reactions and transport behavior within porous electrodes.

INTRODUCTION

As the costs of renewable yet intermittent electricity generation continue to fall, electrochemical systems such as flow batteries have gained attention for potential deployment as grid-scale energy storage units. Significant work has been and continues to be done to improve the performance and ultimately decrease the costs for flow batteries, including adopting potentially inexpensive, earth-abundant aqueous-soluble active materials, developing highly selective, high conductivity, inexpensive ion exchange membranes (IEMs), and modifying commercial electrodes for high conductivity, high electrochemically active surface area, and catalytic properties.[1–4] However, the improvements to each of these components often lack a deeper understanding of their overlap, such as the fluid flow and electrochemical reaction distribution of active species within porous electrodes. *In situ* techniques such as fluorescence microscopy can be used to illuminate these microscale phenomena and shed light on opportunities to improve electrochemical flow system performance.[5]

Porous carbon materials in the form of felts, cloths, and papers have been the preferred electrodes in many redox flow batteries (RFBs) due to their high electronic conductivity, high surface area, chemical and mechanical stability, and inhibition of water electrolysis due to kinetic overpotentials. There are a number of schemes for thermal,[6] chemical,[7] and electrochemical pretreatments, and modifications such as laser perforation,[8] decoration with carbon nanotube,[9] and catalyst growth[10] to enhance the electrode surface area,[11] catalytic properties,[12] and wettability.[13] However, all of these electrode preparation and enhancement procedures start with

---

[1] Harvard John A. Paulson School of Engineering and Applied Sciences, Cambridge, MA 02138, USA

[2] Present address: Lawrence Livermore National Lab, Livermore, CA 94550, USA

[3] Present address: The Racah Institute of Physics, The Hebrew University of Jerusalem, Jerusalem 91904, Israel

[4] Lead contact

*Correspondence: maziz@harvard.edu

https://doi.org/10.1016/j.xcrp.2021.100388

Please cite this article in press as: Wong et al., Direct visualization of electrochemical reactions and heterogeneous transport within porous electrodes *in operando* by fluorescence microscopy, Cell Reports Physical Science (2021), https://doi.org/10.1016/j.xcrp.2021.100388

carbon electrodes produced by relatively few suppliers, and most analyses and cell designs assume that these electrodes behave as ideal homogeneous, isotropic, biphasic porous materials for the purposes of determining electrolyte transport. Some significant research measuring and modeling the properties of these porous electrodes *ex situ*[14,15] suggests that a homogeneous Darcy-like model for fluid transport is unlikely to be completely accurate. However, direct *in situ* and *in operando* measurements on the scale of the electrode fibers and pores have been lacking.

Aqueous soluble organic molecules such as quinones have been increasingly studied because of their potential use as abundant, inexpensive active electrolytes for flow batteries.[16–19] Redox-active quinones can also have distinct fluorescence signatures in their oxidized and reduced states;[20] this enables direct, *in situ*, electrochemical reaction-fluid flow mapping of the active electrolytes by light-based techniques such as fluorescence microscopy. In contrast to other *in situ* techniques used to characterize flow batteries,[21,22] fluorescence microscopy is capable of fast (<100 ms), high-resolution (<10 μm) imaging over large areas, enabling a detailed understanding of the electrolyte-electrode interaction. A number of previous reports have coupled fluorescent, redox-active organic molecules with fluorescence microscopy in a technique called fluorescence-enabled electrochemical microscopy (FEM or FEEM) configured as either an indirect[23,24] or direct[25,26] indicator of redox activity. However, none of these reports explore the electrolyte transport within porous carbon electrodes typical of RFBs.

In this work, we use fluorescence microscopy to illuminate the reaction-flow properties of a quinone flow cell *in operando*, examining several different porous carbon electrodes. The results suggest that carbon electrodes exhibit surprisingly heterogeneous behavior on length scales relevant to flow cell operation. This heterogeneity can lead to a non-uniform fluid flow distribution and a diminished utilization of the full electrode surface area. This work shows stagnant zones and regions of flow channeling with length scales extending beyond an order of magnitude greater than the characteristic pore size. Because of the small variance in the Schmidt number (ratio between kinematic viscosity and molecular diffusivity) among most aqueous electrolytes, these findings are broadly independent of the fluorescent molecular species used in this study. This insight provides an opportunity for exploring improved electrode architectures and engineering high-performance porous electrodes for electrochemical flow systems.

RESULTS AND DISCUSSION

Quinone fluorescence mapping

Scanning electron microscopy (SEM) micrographs of SGL 10AA, SGL 39AA, and Toray 060 at the same magnification are depicted in Figure S1. SGL 34AA has morphology indistinguishable from SGL 39AA due to a common fabrication procedure. Carbon filament diameters are reported in Table S1, and average pore diameters are on the order of 50–100 μm. The images demonstrate that the filament morphologies and distribution differ between carbon papers, in particular with the SGL 10AA containing looping filaments, whereas the SGL 39AA and Toray 060 have long, straight filaments, often spanning many centimeters in length. While bulk properties such as porosity are averaged over the whole electrode volume, the SEM images begin to suggest that physical phenomena on the 100 s of microns scale may be significantly influenced by local physical properties. For many electrochemical systems such as flow batteries, the electrode thickness and interdigitated inlet-outlet channel spacing are on this length scale of hundreds of microns to a few millimeters.

Please cite this article in press as: Wong et al., Direct visualization of electrochemical reactions and heterogeneous transport within porous electrodes *in operando* by fluorescence microscopy, Cell Reports Physical Science (2021), https://doi.org/10.1016/j.xcrp.2021.100388

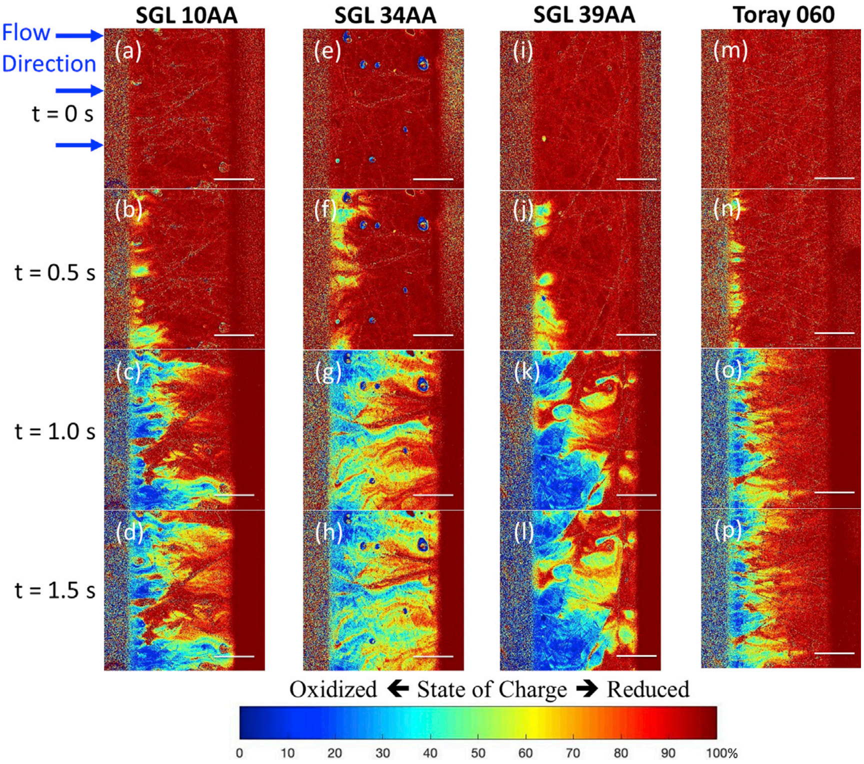

Figure 1. Time-based advection profile through porous carbon electrodes

Time-based advection profile of 4 carbon paper electrodes across the middle land. A 10-mM AQDS electrolyte is fully reduced (red) within the cell at t = 0. Fully oxidized electrolyte (blue) is then forced through the cell with a syringe pump at 100 mL/h (~2.4–3.1 mm/s linear flow rates). As seen in (D) and (H), SGL 10AA and SGL 34AA display strong channeling features, and SGL 39AA (L) has large stagnation regions creating a highly heterogeneous flow profile. Scale bars, 1 mm.

Figure 1 depicts the evolution of fluid flow over time as a fully reduced H_2AQDS (anthraquinone-2,6-disulfonate, red) electrolyte is forced from the land by the inflow of fully oxidized AQDS (blue) electrolytes in each electrode. The figure depicts fluid flow starting at the inlet channel (left) and traversing through the electrode between the membrane and the land (rib of the interdigitated flow field [IDFF]) to the outlet channel (right). These fluorescence microscopy images show non-uniform fluid flow through the electrodes and significant variations in the non-uniformity across different electrode styles despite similarities in their physical properties. The electrolyte state-of-charge (SOC) profiles for the three SGL electrodes in time suggests that these papers are surprisingly heterogeneous in their mass transport properties. The persistent red areas in these images indicate regions of practically stagnant flow where reduced H_2AQDS is not being replenished by the advection of oxidized AQDS. These regions are considered diffusion dominated rather than advection dominated.

While the SGL 10AA, SGL 39AA, and Toray 060 images in Figure 1 show excellent uniformity in electrolyte coverage, the blue circular features in the SGL 34AA electrode images (Figures 1E–1H) indicate trapped bubbles. Entrapped bubbles were often present within the electrodes during assembly, and high velocity electrolyte flow was used to remove as many of them as possible before each experiment. However, some remained persistently entrapped. These have a noticeable impact on the electrolyte flow path and have been observed in previous work on RFBs.[27]

Please cite this article in press as: Wong et al., Direct visualization of electrochemical reactions and heterogeneous transport within porous electrodes *in operando* by fluorescence microscopy, Cell Reports Physical Science (2021), https://doi.org/10.1016/j.xcrp.2021.100388

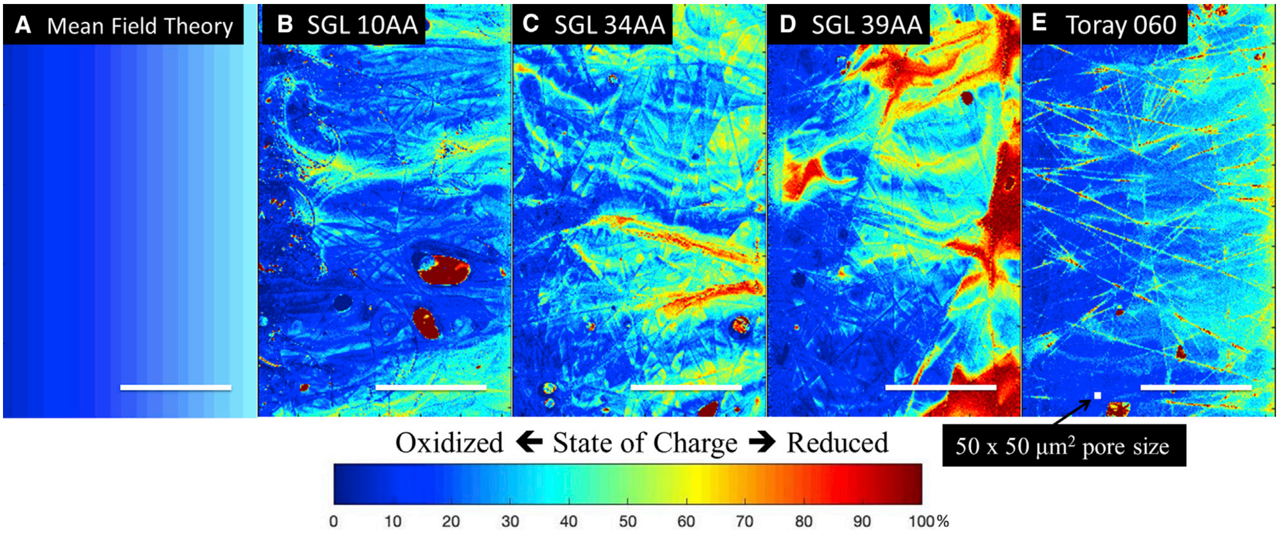

Figure 2. ***Operando* advection-reduction profiles contrasting with mean field theory (MFT) map**

(A–E) (A) Comparison of a MFT calculation to (B–E) 4 porous carbon electrodes during a steady-state reduction of AQDS to H_2AQDS at 60 mA (30 mA/cm^2) with 200 mL/h volumetric flow rate (~5–6 mm/s electrolyte linear flow rate) all across the middle land. The electrolyte utilization is 0.55. In comparison, the SGL electrodes each show strongly heterogeneous behavior, and substantial deviation from the MFT approximation. In (E), a to-scale point representing a typical pore size is featured. Circular red features are bubble artifacts. Scale bars, 1 mm.

Though SGL 39AA and SGL 34AA share similar morphologies, their respective electrolyte reactive-transport profiles display distinctively different behavior, exemplified by contrasting Figures 2C and 2D. In Figure 2, the electrodes are compared during steady-state fluid flow with electrochemical reduction at a constant current, and contrasted with a mean field theory (MFT) approximation. A to-scale point is pictured in Figure 2E, representing a typical 50 × 50 μm^2 pore size. Although the pore size can range substantially, with features up to 100 μm in diameter, the heterogeneities revealed are on length scales an order of magnitude larger. Furthermore, these heterogeneous features are on the length scale of the land width, here, ~2 mm. Because the pore size is over an order of magnitude smaller than the typical land width, MFT approximations assume Darcy-like, homogeneous flow though the electrode.

The MFT assumes one-dimensional (1D) flow at a fixed volumetric flow rate and current density, representing a utilization, U, defined as

$$U = \frac{i\,A}{\dot{Q}\,c\,F\,n}, \qquad \text{(Equation 1)}$$

where i is the current density, A is the IDFF geometric area (2 cm^2), $\dot{Q}$ is the volumetric electrolyte flow rate, F is Faraday's constant (96,485 C/mol), n is the number of transferrable electrons per molecule (AQDS) of reactant (n = 2), and c is the inlet electrolyte concentration (~10 mM).[28] In this approximation, the electrolyte reaction is proportional to the residence time within the electrode, and mass transport limits are not considered. The impact of both $\dot{Q}$ and c on the current and voltage in similar RFBs has been extensively studied in other work.[29–31] The incorporation of U allows for a nondimensional extrapolation of the current density-flow rate-concentration relationship. This low concentration analysis provides expanded insight into low flow rate and high utilization regimes that are uncommon for many electrochemical flow systems. The land alone is shown for comparison to the experimental measurements, although the MFT extends to the centerlines of both the inlet and outlet

Please cite this article in press as: Wong et al., Direct visualization of electrochemical reactions and heterogeneous transport within porous electrodes *in operando* by fluorescence microscopy, Cell Reports Physical Science (2021), https://doi.org/10.1016/j.xcrp.2021.100388

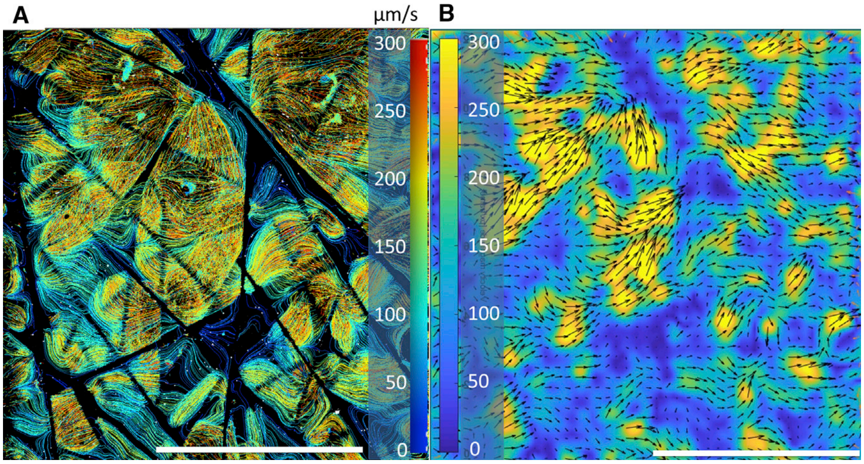

Figure 3. Fluorescent particle flow imaging within a porous carbon electrode

(A) Particle tracing velocity map and (B) PIV map of electrolyte transport within an SGL 39AA electrode at a 10 mL/h volumetric flow rate (~300 μm/s linear flow rate). Both figures use the same data. Images are taken at the middle land with the bulk flow from left to right. Scale bars, 500 μm.

channels, commensurate with previous numerical analyses of RFB channels and lands.[31] The pronounced dichotomy between MFT and experimental results is illustrated even more sharply in Figure S2 and discussed in Note S1. These results challenge the practice that a homogeneous Darcy-like permeability-flow assumption is sufficient for flow cell modeling, and suggest that more complete reaction-flow models are needed to more accurately capture the transport physics within electrochemical flow cells. Recent multidimensional computational models have enabled new insight into the significant impact of localized geometries on electrochemical reaction-flow properties.[32,33] These models have been used to corroborate experimental bulk electrochemical results with high fidelity. This fluorescence microscopy technique provides an experimental tool for testing and enhancing advanced computational models.

Fluorescent tracer particle mapping

Using fluorescence microscopy particle tracing, the local electrolyte velocity field within a porous electrode is imaged independently of the electrolyte fluorescence. The quantified fluid velocity field within an SGL 39AA electrode is shown in Figure 3. Although this technique is biased toward fluid motion closest to the microscope objective, the distinct heterogeneity in flow is again observed. The fully dark lines in Figure 3A are regions where the electrode fibers shadow particles flowing beneath, but serve as guides to observe the spatial distribution of velocity within individual pores, namely regions of slow transport (dark blue) adjacent to the fibers and regions of rapid transport (red) along the pore centerline. We note that these maps constitute a 2D x-y velocity profile but indicate substantial transport in the z direction due to the particle divergence into and out of the field of view. Although not discernible from these images, transport in the z direction is clearly observable by this technique, providing opportunities for 3D techniques such as confocal microscopy to measure multi-dimensional mass transport with high spatial resolution.

Given the surprisingly heterogeneous electrolyte transport properties within these porous carbon paper electrodes observed from both electrolyte SOC and velocity maps, the impact of flow field geometry on electrolyte transport becomes an

Please cite this article in press as: Wong et al., Direct visualization of electrochemical reactions and heterogeneous transport within porous electrodes *in operando* by fluorescence microscopy, Cell Reports Physical Science (2021), https://doi.org/10.1016/j.xcrp.2021.100388

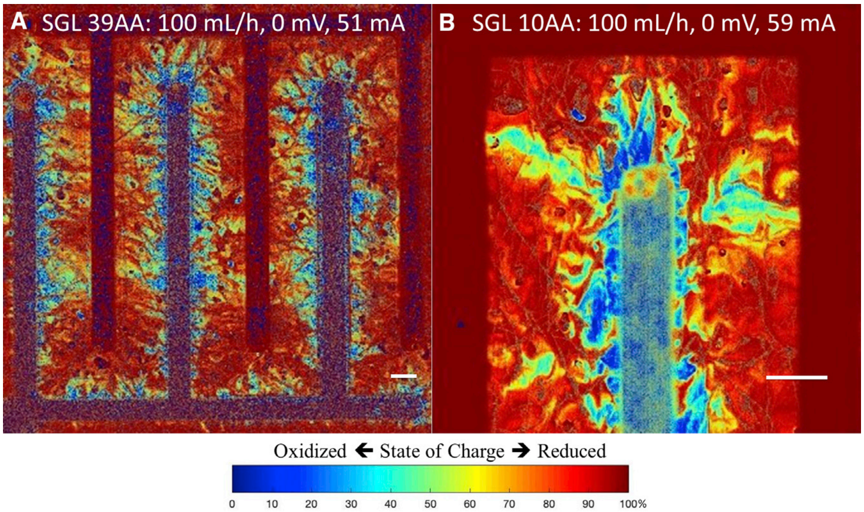

Figure 4. Spatial flow field-porous electrode flow profiles

(A and B) Steady-state reaction-flow maps of AQDS reduction to H_2AQDS with an SGL 10AA electrode across (A) the full 2 cm^2 IDFF and (B) at an inlet digit end. Average currents are reported in each panel. These images have been averaged over a stack of 150 images, yielding excellent resolution. A significant number of bubble-induced artifacts can be observed in both images. Scale bars, 1 mm.

important aspect to consider. Most 1D and MFT models assume uniform, linear electrolyte flow from the IDFF high-pressure inlet to the low-pressure outlet, which has already been demonstrated to be inaccurate in the systems described here. Flow fields designed with high aspect ratios favoring long parallel channels better approximate this assumption. However, the effect of electrolyte flowing from the digit end of an inlet finger to a U-shaped outlet is not well understood.

Flow field-porous electrode interactions

To gain highly resolved reaction-flow map, a series of frames during steady-state experiments with constant electrolyte flow and applied current is averaged, reducing the signal-to-noise. In Figure 4A, the regularity of the flow pattern at the digit end depicted in Figure 4B becomes more pronounced as seen by the deep red regions of reduced H_2AQDS at the end of the outlet fingers. High-resolution images such as these can enable deep probing of electrolyte advection-diffusion flow profiles within a variety of porous electrodes. Figures S3 and S4 further show the transient behavior of the electrolyte flow profile at the inlet digit end and within the entire IDFF, respectively, as discussed in Notes S2 and S3. These transient profiles depict long-lived diffusion-limited regions both along the land and within the IDFF channel corners, suggesting that the IDFF geometry and the electrode structure have an interdependent relationship that significantly influences mass transport (see Video S1).

Coupled fluorescence mapping and electrochemical reduction

Combining fluorescence microscopy with steady-state electrical current and fluid flow rate enables a full map of the accessible operating conditions for redox active electrolytes within a given electrode. Figure 5 displays the reaction-flow profile of SGL 10AA across a range of flow rates and applied currents. Comparing the final frame in each column, characteristics can be identified as indicative of mass transport-limiting effects, including the onset of a highly reduced diffusion-dominated region. Figure 5B shows the I-V polarization data corresponding to each figure. At

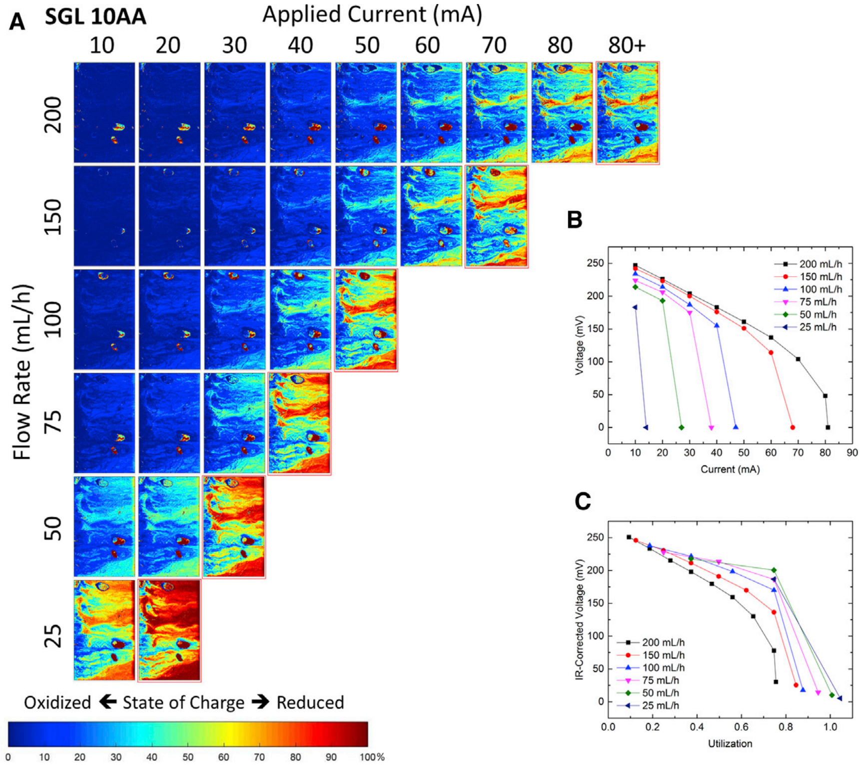

Figure 5. Flow profiles with coupled steady-state advection and constant current reduction

(A) Steady-state fluorescence maps of 10 mM AQDS through SGL 10AA along a middle land, varying the electrolyte volumetric flow rate and applied current. The last figure in each row, indicated by a red border, is measured potentiostatically at 0 mV rather than galvanostatically.

(B) Voltage versus current polarization plot corresponding to the steady-state condition for each image.

(C) iR-corrected voltage as functions of utilization assuming 10 mM, 2-electron reduction AQDS solution (Equation 1). Data with utilization >1 suggest slight variations in electrolyte concentration or minor side reactions.

increasing flow rates, the onset of the mass transport overpotential, characterized by the sharp decrease in voltage over a small range of currents, extends to larger currents. As described in previous work,[28] subtracting the high-frequency resistance (a convolution of electrode, electrolyte, and membrane ohmic and electrokinetic resistances) and normalizing the current to an electrolyte utilization from Equation 1, a polarization curve of iR-corrected voltage and utilization is created as shown in Figure 5C.

Because the mass transport overpotential in tortuous electrodes contains within it a diffusion rate, the longer residence times allowed by the experiments at smaller volumetric flow rates are able to access a higher electrolyte utilization. We note that because the calculation of utilization is normalized assuming a 10-mM electrolyte concentration, the appearance of electrolytes with a utilization >1 is likely due to small deviations in the true electrolyte concentration or minor competing side reactions such as hydrogen evolution. While this difference in concentration will affect the normalization leading to the utilization value, the fluorescence normalization procedure is concentration agnostic, barring significant optical attenuation of the electrolyte. Absorption properties of AQDS electrolytes have been explored in previous work.[29] Figure S5 reports the same analysis for the MFT approximation, and

Figures S6–S8 display the comparable fluorescence maps for the SGL 34AA, SGL 39AA, and 2xToray 060 experiments, respectively. These comparisons are discussed further in Notes S4 and S5.

In this work, we explore the use of direct visualization of AQDS reaction flow within porous carbon electrodes using fluorescence microscopy. This technique enables new insights into electrochemical reaction-flow properties due to its high temporal (<100 ms) and spatial (<10 μm) resolutions. We measure both electrolyte (SOC) and electrolyte velocity fields, and create both steady-state and transient spatial maps of these properties within porous carbon electrodes, spanning from flow within individual pores to reactions across a full flow field. Fluorescence microscopy performed while physically displacing reduced H_2AQDS by flowing oxidized AQDS within porous carbon papers shows a significant electrolyte channeling effect, creating high-flow, advection-dominated regions and low-flow, diffusion-dominated regions. This work demonstrates that despite having similar morphologies, many porous carbon electrodes have starkly different flow properties at length scales that extend an order of magnitude larger than the characteristic pore size. These findings indicate a complicated relationship between Darcy-like bulk properties such as porosity and permeability and microscale properties such as surface area and spatial correlations in structure.

Through connecting fluorescence maps with electrochemical polarization, our work demonstrates how fluorescence microscopy *in operando* opens the possibility of evaluating engineered high-performance porous electrodes. Both steady-state and transient electrochemical experiments further demonstrate that electrolyte SOC distribution across many porous electrodes is substantially heterogeneous, characterized by localized stagnant zones and hydraulic electrolyte channeling. In addition, this technique demonstrates how the flow field geometry can exacerbate heterogeneities in electrolyte distribution. The heterogeneous flow within porous electrodes is correlated to a diminished performance of assembled cells and may persist for electrochemical systems such as flow batteries operating at scale. This technique can be extended to explore the impact of different porous electrode styles, geometries, compressions, orientations, and features on localized electrochemical reaction-flow properties, providing new insight into the mass transport limitations within these structures. We infer that electrode designs that lead to more homogeneous electrolyte distribution, and therefore a greater utilization of the porous electrode surface area, will lead to improved electrochemical performance of high-power density electrochemical systems.

EXPERIMENTAL PROCEDURES

Resource availability

Lead contact

Further information and requests for resources should be directed to the lead contact, Michael J. Aziz (maziz@harvard.edu)

Materials availability

This research did not generate any unique materials.

Data and code availability

This research did not generate any code. All of the data associated with this research are represented in this manuscript and supplemental information. Other data are available from the lead contact upon reasonable request.

Please cite this article in press as: Wong et al., Direct visualization of electrochemical reactions and heterogeneous transport within porous electrodes *in operando* by fluorescence microscopy, Cell Reports Physical Science (2021), https://doi.org/10.1016/j.xcrp.2021.100388

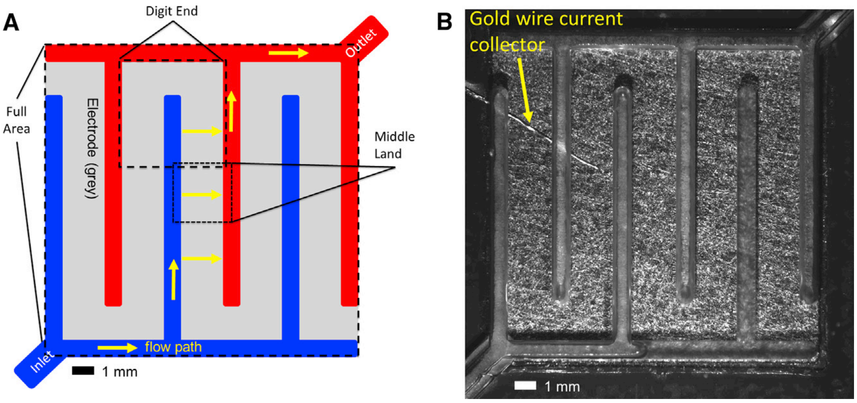

Figure 6. Flow field-porous electrode schematic and image

(A) Schematic of the 2 cm^2 interdigitated flow field (IDFF), highlighting the fluid flow path from the high-pressure inlet, through the carbon electrode underneath the land, and out the low-pressure outlet. Three regions of interest are marked with dashed lines, corresponding to particular imaging experiments.

(B) Bright-field optical microscopy image of the IDFF on top of a porous carbon electrode. A gold wire current collector connects the electrode to an external circuit.

Experimental setup

A homemade quinone-hydrogen flow cell (QHFC) is used for all of the fluorescence microscopy experiments, and is pictured and drawn schematically in Figure S9. The negative terminal is plumbed with a pressurized, humidified hydrogen source regulated to an inlet pressure of 5 psi. Hydrogen is oxidized (hydrogen oxidation reaction [HOR]) at the 5 cm^2 negative electrode (Pt-C reformate anode, Alfa Aesar) compressed against a stainless-steel current collector with a grooved serpentine flow field to enable excess liquid removal to prevent flooding. The positive terminal is plumbed with 10 mM AQDS in 1 M H_2SO_4. The active species concentration is limited to 10 mM due to the strong optical attenuation of the reduced and oxidized AQDS species and of the quinhydrone dimer that forms at higher concentrations and intermediate SOCs.[29] At lower concentrations, the relationship between fluorescence intensity and SOC remains linear although the signal-to-noise ratio diminishes with decreasing concentration. In contrast to its use in other flow battery literature,[16,30] here, the AQDS electrolyte is called the posolyte due to its positive redox potential compared to HOR. AQDS is reduced to H_2AQDS as it flows within a porous carbon electrode compressed against a gold wire current collector. Measurements with a gold wire mesh current collector, used to enhance spatial current uniformity, were hindered by substantial electrolyte channeling between the electrode and the mesh. Although slight current distribution variation was observed within the carbon paper under transient operation, full area mapping of the electrode reaction does not exhibit quantitative variation in the steady-state current distribution.

A Nafion 212 cation exchange membrane (CEM) is used to separate the two half-cell reactions. A 2-cm^2 IDFF is milled out of 3/16″ UV-transparent acrylic (clear UV-transmitting [UVT] acrylic, EMCO Industrial Plastics) and assembled on top of the positive terminal to enable direct visualization with microscopy. Figure 6 depicts a schematic and a bright-field micrograph of the IDFF on top of the positive electrode. Fluid transport proceeds through the flow field channels and across the land such that all of the electrolyte must flow through the electrode for ~2 mm to reach an outlet channel.

Please cite this article in press as: Wong et al., Direct visualization of electrochemical reactions and heterogeneous transport within porous electrodes *in operando* by fluorescence microscopy, Cell Reports Physical Science (2021), https://doi.org/10.1016/j.xcrp.2021.100388

Porous electrodes

Four porous carbon papers, Sigracet 10AA, 34AA and 39AA (SGL Carbon), and Toray 060, are used for the positive electrode. This technique is amenable to a wide range of porous electrode materials, assuming the filament packing density enables line-of-sight illumination of the internal pore structure. The Sigracet carbon papers are pretreated by baking at 400°C in air for 24 h, and the Toray 060 is pretreated by chemical etching in a 1:3 (v:v) mixture of concentrated nitric and sulfuric acids for 5 h at 50°C following the procedure described by Chen et al.[18] Table S1 gives the physical properties of each porous carbon paper electrode. Two layers of Toray 060 are used in the experiments to match the thickness of the SGL papers.

The compressed thicknesses of the porous carbon papers are controlled by polytetrafluoroethylene (PTFE) gasket spacers. Spacers of 200 μm (0.008″) are used for SGL 34AA and 39AA to compress each electrode to 29% engineering strain, and 280 μm (0.011″) spacers are used for SGL 10AA and 2-layer Toray 060 to compress the electrodes to 28% and 26% engineering strain, respectively, between the UVT acrylic flow plate and the CEM. This range of compressions is selected to align with other comparable electrode compressive strains in the literature.[34] Although there are several different flow field designs for electrochemical flow systems,[35] and this method is readily applicable to imaging the electrode reaction-flow profiles using each of them, the IDFF geometry (Figure 6) was selected to image the total fluid flow through lands of the electrode. In contrast to flow-by designs, this configuration prevents fluid from bypassing the electrode. The flow field design and the electrode morphology both influence the fluid-flow and electrochemical reactions and are expected to affect the ultimate device performance.

The electrolyte linear flow rate u_0 is calculated assuming a volumetric flow rate Q_0 passes uniformly from the channel into the electrode along a channel-land perimeter, P, measured in this 2 cm^2 IDFF to be ~68 mm. The resulting cross-sectional area for fluid transport through the porous electrode is given as Pt, where t is the compressed electrode thickness, determined by the gasket thickness. Therefore, the average linear flow rate can be approximated as

$$u_0 \approx \frac{Q_0}{Pt}\left\{1 - \frac{(1-\phi)}{(1-\varepsilon)}\right\}^{-1} \qquad \text{(Equation 2)}$$

where ϕ is the porosity (void fraction) of the uncompressed electrode giving $(1-\phi)$ as the solid fraction, and ε is the engineering compressive strain on the electrode, leading to $(1-\varepsilon)$ as the normalized compressed thickness. Therefore, $(1-\phi)/(1-\varepsilon)$ is the compressed solid fraction and $\{1-(1-\phi)/(1-\varepsilon)\}$ is the compressed void fraction. The compressed void fractions (porosities) for these experiments are 0.75 for SGL 10AA, 0.65 for SGL 34AA, 0.85 for SGL 39AA, and 0.70 for 2xToray 060. All of the porosity values are calculated assuming literature values of intrinsic porosities and thicknesses listed in Table S1 for uncompressed electrodes (i.e., $\varepsilon = 0$) and a zero solid fraction change when compressed to the thickness of the gasket. A study on the pretreatment of similar porous carbon electrodes shows negligible variation between pristine electrodes and electrodes heat treated at 400°C.[36] The smaller the compressed void fraction, the greater the linear flow rate due to the same volumetric flow constrained to a smaller cross-sectional area. Because of the assumption that the engineering strain cannot compress the solid material, the relationship is constrained to conditions in which $\phi - \varepsilon > 0$.

Please cite this article in press as: Wong et al., Direct visualization of electrochemical reactions and heterogeneous transport within porous electrodes *in operando* by fluorescence microscopy, Cell Reports Physical Science (2021), https://doi.org/10.1016/j.xcrp.2021.100388

Flow and electrochemical parameters

The two prominent operating parameters influencing electrolyte reactive transport are volumetric flow rate and applied current. The latter can be a function of operating voltage or power. While the electrode operating voltage will affect the electric field between the cathode and the anode, the concentrated supporting electrolyte significantly reduces the Debye screening length between the electrode surface and the electrolyte bulk, negating electrostatic species transport within the porous electrode. All of the electrochemical experiments are performed nominally at room temperature with a Gamry Reference 3000 Potentiostat. The posolyte is circulated using a syringe pump unless indicated as a peristaltic pump (Cole Parmer, MasterFlex). The open circuit voltage is ~+250 mV and the reduction of AQDS to H_2AQDS is a spontaneous process when paired with the HOR. Electrochemical conditions for each experiment are described in the Results and discussion section. All of the electrical current measurements are given as an absolute value, with a greater current indicating a more rapid reduction of AQDS. The full assembly is imaged through a fluorescence microscope (Axio Zoom V.16, Filter Set 02, Plan Neofluar 1× objective) with a 50-fps (50 Hz) capture rate. The image processing procedure to determine a local SOC for all of these experiments is outlined in Figure S10 and discussed in Note S6. The image processing procedure is applicable under the operating conditions described here due to the linear relationship between fluorescence intensity and electrolyte SOC depicted in Figure S11.

Electrolyte velocity measurements use 1 μm neutrally buoyant fluorescent tracer particles flowing through the porous electrodes. Tracer particle sequences are normalized using an image processing procedure similar to that of the SOC mapping to remove background noise. We explore two methods of quantifying fluid velocity: calibrated frame-based particle tracing (ImageJ software) and particle image velocimetry (PIV, MATLAB PIVlab software). PIV velocity fields are produced by comparing the relative, aggregate particle motion between sequential frame pairs in a time series image stack. These velocity fields can be averaged to generate a single velocity vector map.

SUPPLEMENTAL INFORMATION

Supplemental information can be found online at https://doi.org/10.1016/j.xcrp.2021.100388.

ACKNOWLEDGMENTS

This research was supported initially by US Department of Energy (DOE) award DE-AC05-76RL01830 through PNNL subcontract 428977 and subsequently by the US DOE Office of Basic Energy Sciences award DE-SC0020170. Manuscript preparation was performed by A.A.W. under the auspices of the US DOE by Lawrence Livermore National Laboratory under contract DE-AC52-07NA27344. The authors thank Anton Graf for helpful discussions.

AUTHOR CONTRIBUTIONS

A.A.W. performed all of the experiments, image processing, and data analysis, and drafted the manuscript. S.M.R. advised on the imaging procedure, provided the fluorescence microscopy equipment, and contributed to the editing of the manuscript. M.J.A. advised on the overall project, guided the computational modeling, secured the funding, provided the electrochemical equipment, and contributed to the editing of the manuscript.

Please cite this article in press as: Wong et al., Direct visualization of electrochemical reactions and heterogeneous transport within porous electrodes *in operando* by fluorescence microscopy, Cell Reports Physical Science (2021), https://doi.org/10.1016/j.xcrp.2021.100388

DECLARATION OF INTERESTS

The authors declare no competing interests.

Received: January 8, 2021
Revised: February 12, 2021
Accepted: March 4, 2021
Published: March 25, 2021

REFERENCES

1. Soloveichik, G.L. (2015). Flow Batteries: Current Status and Trends. Chem. Rev. *115*, 11533–11558.
2. Perry, M.L., and Weber, A.Z. (2016). Advanced Redox-Flow Batteries: A Perspective. J. Electrochem. Soc. *163*, A5064–A5067.
3. Park, M., Ryu, J., Wang, W., and Cho, J. (2017). Material design and engineering of next-generation flow-battery technologies. Nat. Rev. Mater. *2*, 16080.
4. Winsberg, J., Hagemann, T., Janoschka, T., Hager, M.D., and Schubert, U.S. (2017). Redox-Flow Batteries: From Metals to Organic Redox-Active Materials. Angew. Chem. Int. Ed. Engl. *56*, 686–711.
5. Bazylak, A. (2009). Liquid water visualization in PEM fuel cells: a review. Int. J. Hydrogen Energy *34*, 3845–3857.
6. Park, J.H., Park, J.J., Park, O.O., Jin, C.-S., and Yang, J.H. (2016). Highly accurate apparatus for electrochemical characterization of the felt electrodes used in redox flow batteries. J. Power Sources *310*, 137–144.
7. Yarlagadda, V., and Nguyen, T.V. (2016). High Surface Area Carbon Electrodes for the Bromine Reactions in H_2-Br_2 Fuel Cells. J. Electrochem. Soc. *163*, A5126–A5133.
8. Mayrhuber, I., Dennison, C.R., Kalra, V., and Kumbur, E.C. (2014). Laser-perforated carbon paper electrodes for improved mass-transport in high power density vanadium redox flow batteries. J. Power Sources *260*, 251–258.
9. Yuan, D., Zhu, Y.G., and Jia, C. (2016). Carbon Nanotube-Polymer Composites for Energy Storage Applications. Carbon Nanotubes - Current Progress of Their Polymer Composites (IntechOpen).
10. Wei, L., Zhao, T., Zeng, L., and Jiang, H. (2017). Highly catalytic and stabilized titanium nitride nanowire array-decorated graphite felt electrodes for all vanadium redox flow batteries. J. Power Sources *341*, 318–326.
11. Liu, T., Li, X., Xu, C., and Zhang, H. (2017). Activated Carbon Fiber Paper Based Electrodes with High Electrocatalytic Activity for Vanadium Flow Batteries with Improved Power Density. ACS Appl. Mater. Interfaces *9*, 4626–4633.
12. Park, J.J., Park, J.H., Park, O.O., and Yang, J.H. (2016). Highly porous graphenated graphite felt electrodes with catalytic defects for high-performance vanadium redox flow batteries produced via NiO/Ni redox reactions. Carbon *11*, 17–26.
13. Zhang, Z., Xi, J., Zhou, H., and Qiu, X. (2016). KOH etched graphite felt with improved wettability and activity for vanadium flow batteries. Electrochim. Acta *218*, 15–23.
14. Qiu, G., Dennison, C.R., Knehr, K.W., Kumbur, E.C., and Sun, Y. (2012). Pore-scale analysis of effects of electrode morphology and electrolyte flow conditions on performance of vanadium redox flow batteries. J. Power Sources *219*, 223–234.
15. Qiu, G., Joshi, A.S., Dennison, C.R., Knehr, K.W., Kumbur, E.C., and Sun, Y. (2012). 3-D pore-scale resolved model for coupled species/charge/fluid transport in a vanadium redox flow battery. Electrochim. Acta *64*, 46–64.
16. Huskinson, B., Marshak, M.P., Suh, C., Er, S., Gerhardt, M.R., Galvin, C.J., Chen, X., Aspuru-Guzik, A., Gordon, R.G., and Aziz, M.J. (2014). A metal-free organic-inorganic aqueous flow battery. Nature *505*, 195–198.
17. Lin, K., Chen, Q., Gerhardt, M.R., Tong, L., Kim, S.B., Eisenach, L., Valle, A.W., Hardee, D., Gordon, R.G., Aziz, M.J., and Marshak, M.P. (2015). Alkaline quinone flow battery. Science *349*, 1529–1532.
18. Chen, Q., Eisenach, L., and Aziz, M.J. (2015). Cycling Analysis of a Quinone-Bromide Redox Flow Battery. J. Electrochem. Soc. *163*, A5057–A5063.
19. Hoober-Burkhardt, L., Krishnamoorthy, S., Yang, B., Murali, A., Nirmalchandar, A.S., Prakash, G.K., and Narayanan, S.R. (2017). A New Michael-Reaction-Resistant Benzoquinone for Aqueous Organic Redox Flow Batteries. J. Electrochem. Soc. *164*, A600–A607.
20. Cory, R.M., and McKnight, D.M. (2005). Fluorescence spectroscopy reveals ubiquitous presence of oxidized and reduced quinones in dissolved organic matter. Environ. Sci. Technol. *39*, 8142–8149.
21. Clement, J.T., Aaron, D.S., and Mench, M.M. (2015). In Situ Localized Current Distribution Measurements in All-Vanadium Redox Flow Batteries. J. Electrochem. Soc. *163*, A5220–A5228.
22. Gandomi, Y.A., Aaron, D.S., Houser, J.R., Daugherty, M.C., Clement, J.T., Pezeshki, A.M., Ertugrul, T.Y., Moseley, D.P., and Mench, M.M. (2018). Critical Review—Experimental Diagnostics and Material Characterization Techniques Used on Redox Flow Batteries. J. Electrochem. Soc. *165*, A970–A1010.
23. Pruchyathamkorn, J., Yang, M., Amin, H.M.A., Batchelor-McAuley, C., and Compton, R.G. (2017). Imaging Electrode Heterogeneity Using Chemically Confined Fluorescence Electrochemical Microscopy. J. Phys. Chem. Lett. *8*, 6124–6127.
24. Oja, S.M., and Zhang, B. (2014). Imaging transient formation of diffusion layers with fluorescence-enabled electrochemical microscopy. Anal. Chem. *86*, 12299–12307.
25. Miomandre, F., Meallet-Renault, R., Vachon, J.-J., Pansu, R.B., and Audebert, P. (2008). Fluorescence microscopy coupled to electrochemistry: a powerful tool for the controlled electrochemical switch of fluorescent molecules. Chem. Commun. (Camb.) (16), 1913–1915.
26. Bouffier, L., and Doneaux, T. (2017). Coupling electrochemistry with in situ fluorescence (confocal) microscopy. Curr. Opin. Electrochem. *6*, 31–37.
27. Bevilacqua, N., Eifert, L., Banerjee, R., Köble, K., Faragó, T., Zuber, M., Bazylak, A., and Zeis, R. (2019). Visualization of electrolyte flow in vanadium redox flow batteries using synchrotron X-ray radiography and tomography – impact of electrolyte species and electrode compression. J. Power Sources *439*, 1–10.
28. Wong, A.A., and Aziz, M.J. (2020). Method for Comparing Porous Carbon Electrode Performance in Redox Flow Batteries. J. Electrochem. Soc. *167*, 110542.
29. Tong, L., Chen, Q., Wong, A.A., Gómez-Bombarelli, R., Aspuru-Guzik, A., Gordon, R.G., and Aziz, M.J. (2017). UV-Vis spectrophotometry of quinone flow battery electrolyte for in situ monitoring and improved electrochemical modeling of potential and quinhydrone formation. Phys. Chem. Chem. Phys. *19*, 31684–31691.
30. Chen, Q., Gerhardt, M.R., and Aziz, M.J. (2017). Dissection of the Voltage Losses of an Acidic Quinone Redox Flow Battery. J. Electrochem. Soc. *164*, A1126–A1132.
31. Gerhardt, M.R., Wong, A.A., and Aziz, M.J. (2018). The Effect of Interdigitated Channel and Land Dimensions on Flow Cell Performance. J. Electrochem. Soc. *165*, A2625–A2643.
32. Zhang, D., Forner-Cuenca, A., Taiwo, O., Yufit, V., Brushett, F., Brandon, N., Gu, S., and Cai, Q. (2020). Understanding the role of the porous electrode microstructure in redox flow battery

performance using an experimentally validated 3D pore-scale lattice Boltzmann model. J. Power Sources *447*, 227249.

33. Sadeghi, M.A., Aganou, M., Kok, M., Aghighi, M., Merle, G., Barralet, J., and Gostick, J. (2019). Exploring the Impact of Electrode Microstructure on Redox Flow Battery Performance Using a Multiphysics Pore Network Model. J. Electrochem. Soc. *166*, A2121–A2130.
34. Ghimire, P.C., Bhattari, A., Schweiss, R., Scherer, G.G., Wai, N., and Yan, Q. (2018). A comprehensive study of electrode compression effects in all vanadium redox flow batteries including locally resolved measurements. Appl. Energy *230*, 974–982.
35. Darling, R.M., and Perry, M.L. (2014). The Influence of Electrode and Channel Configurations on Flow Battery Performance. J. Electrochem. Soc. *161*, A1381–A1387.
36. Greco, K.V., Forner-Cuenca, A., Mularczyk, A., Eller, J., and Brushett, F.R. (2018). Elucidating the Nuanced Effects of Thermal Pretreatment on Carbon Paper Electrodes for Vanadium Redox Flow Batteries. ACS Appl. Mater. Interfaces *10*, 44430–44442.

Cell Reports Physical Science, Volume *2*

Supplemental information

Direct visualization of electrochemical reactions and heterogeneous transport within porous electrodes *in operando* by fluorescence microscopy

Andrew A. Wong, Shmuel M. Rubinstein, and Michael J. Aziz

Supplemental Items

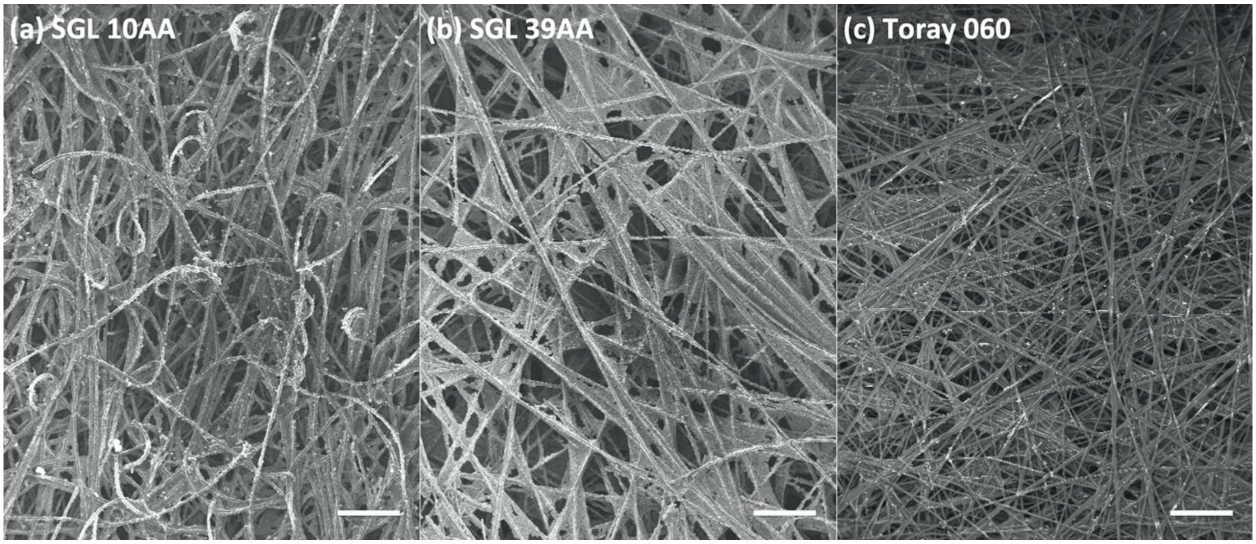

Figure S1. **SEM micrographs of porous carbon paper electrodes**. (a) SGL 10AA, (b) SGL 39AA and (c) Toray 060. SGL 34AA has a similar morphology to SGL 39AA due to a common fabrication procedure. All scale bars are 100 µm.

Table S1. **Porous carbon electrode comparison**. Comparison of porous carbon paper electrode physical properties as specified by the manufacturer. *Asterisk indicates own measurement

Physical Property	SGL 10AA	SGL 34AA	SGL 39AA	Toray 060
Thickness (µm)	390	280	280	190
Porosity (%)	82	75	89	78
Through-Plane ASR (mΩ cm^2)	<16	<14	<5	80
Fiber Diameter (µm)*	10	8	8	10

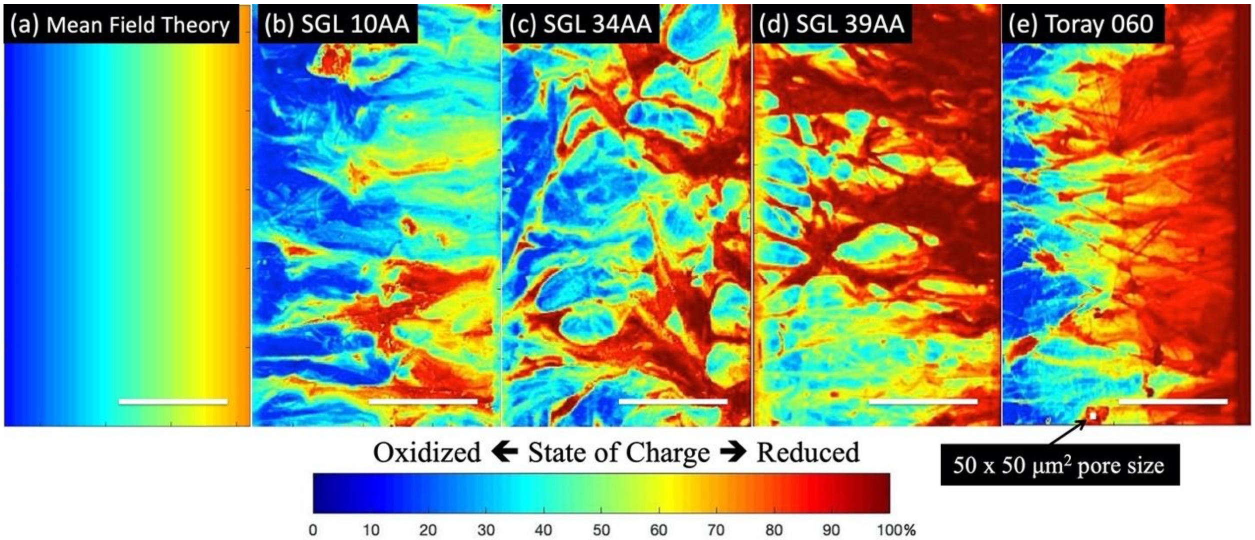

Figure S2. **Fluorescence advection profiles through porous carbon electrodes compared to mean field theory calculation.** Colorized fluorescence images of the middle land with a constant voltage (0 mV) during a peristaltic pump pulsed flow, showing reduced vs. oxidized electrolyte distribution in space. The dramatic heterogeneities stand in sharp contrast to a representative mean field theory approximation. In (e), a to-scale point representing a typical pore size is featured. For comparison, the mean pore diameter for SGL 39AA is ~44 um uncompressed. All scale bars are 1 mm.

Note S1

The contrast between the MFT and the experimental results further suggests that spatial variations in fluid flow and electrochemical reactions are important considerations in the operation and performance of RFBs. To show the contrast more sharply, the images in Figure S2 are obtained during the electrochemical reduction of AQDS at 0 mV while the electrolyte is fed via a peristaltic pump as a pulsed flow. The MFT approximation in Figure S2(a) is a representative of nearly complete electrolyte utilization. At high utilization rates, striking heterogeneities across all electrode styles become evident. Despite the similar morphologies between SGL 39AA and Toray 060 as indicated from Figure S1. , it is evident from Figure S2 that the advective mass transport differs significantly between the two. The differences in these properties could be due to a number of factors including surface wettability and through-plane electrode morphology that is not captured by these 2D imaging techniques.

In Figure S2(e), a to-scale point is pictured, representing a typical 50 x 50 µm^2 pore size obtained from SEM micrographs. Though the pore size can range substantially, with features up to 100 µm in diameter, the heterogeneities depicted are on length scales an order of magnitude larger. Furthermore, these heterogeneous features are on the length scale of the land width, here ~2 mm. Because the pore size is over an order of magnitude smaller than the typical land width, and the flows are within a steady regime, MFT approximations assume Darcy-like flow though the electrode.

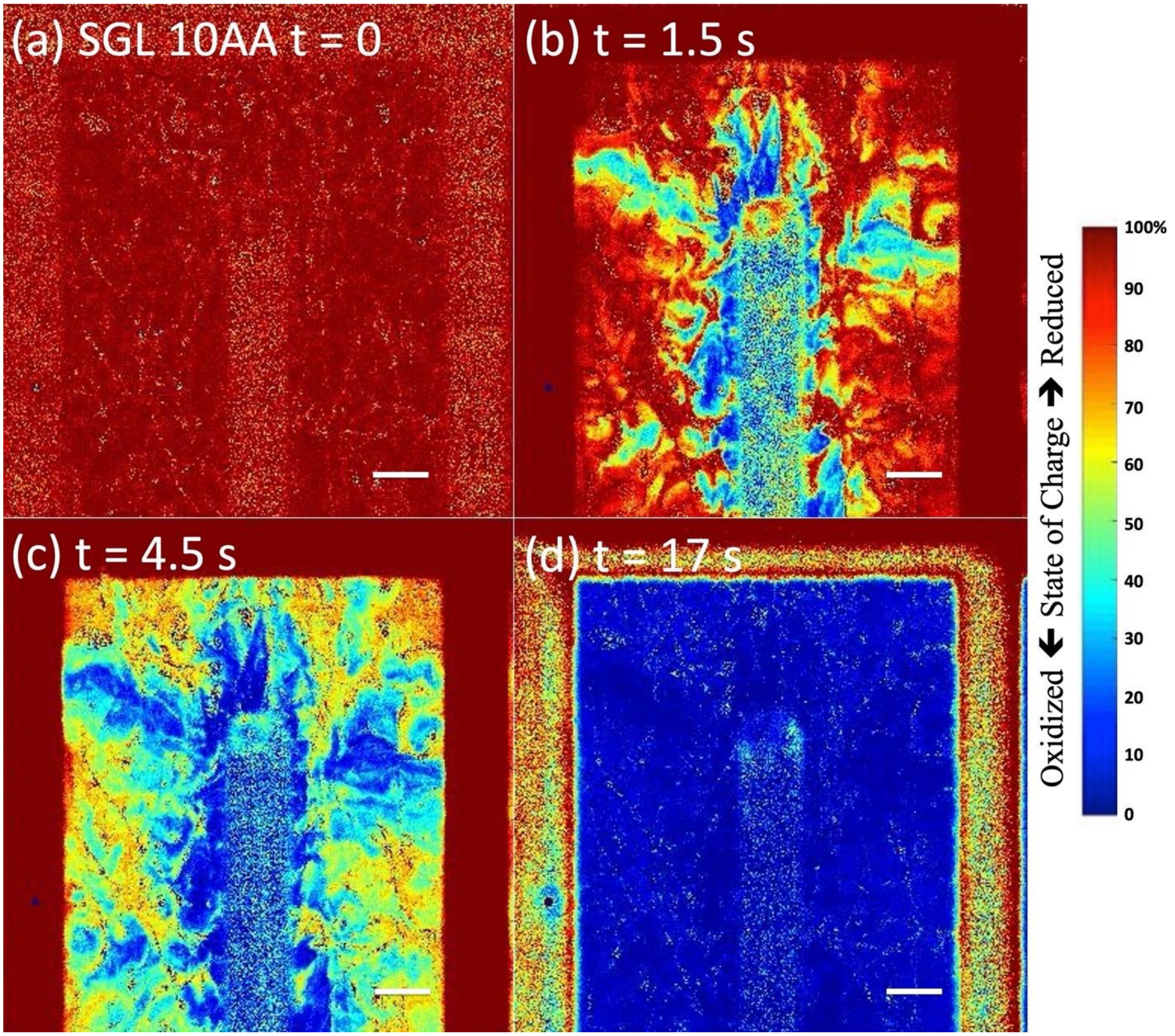

Figure S3. **Time evolution of electrolyte advection-diffusion at a flow field digit end.** Fluorescence microscope images of an inlet channel digit end location distributing oxidized AQDS into SGL 10AA carbon paper over time. Fluid flow is 100 mL/h (2.7 mm/s across the land) and no current is passed. The dark blue regions are areas of more rapid electrolyte fluid flow and suggest pathways of lower pressure drops. Scale bars are 1 mm.

Note S2

Figure S3 shows the flow map of the inlet finger of the IDFF over an SGL 10AA carbon paper. Identical to the experiment depicted in Figure 2, fully reduced H_2AQDS electrolyte is displaced by oxidized AQDS. Distinct dark blue channels extending vertically and horizontally from the digit end indicate regions that are more rapidly refreshed by the advection of oxidized AQDS. This is somewhat unsurprising given that the shortest paths between inlet and outlet are at these angles. We note that while the inlet channel has a dark region of oxidized AQDS on its border, the channeling effect within the first few hundred microns through the land are determined by the electrode morphology. This result highlights that although it is important to design flow fields for optimized fluid distribution to the electrode, the local reactant distribution might be strongly dependent on the electrode geometry and morphology, suggesting that this can also be optimized.

Though less clear and not explored in depth in this work, Figure S3(d) indicates that fluid flow within the channel can also be imaged, shedding light on the co-laminar flow interaction within the channel. Because the acrylic IDFF used here is fabricated using a CNC end mill, the surface is translucent, allowing diffuse transmittance of light and enabling approximate measurements but obscuring details. Developing a process to smooth the channel groves may open opportunities to directly observe the electrolyte entering into the electrode and monitor the effects of electrode protruding into the channel as has been explored in other work[1].

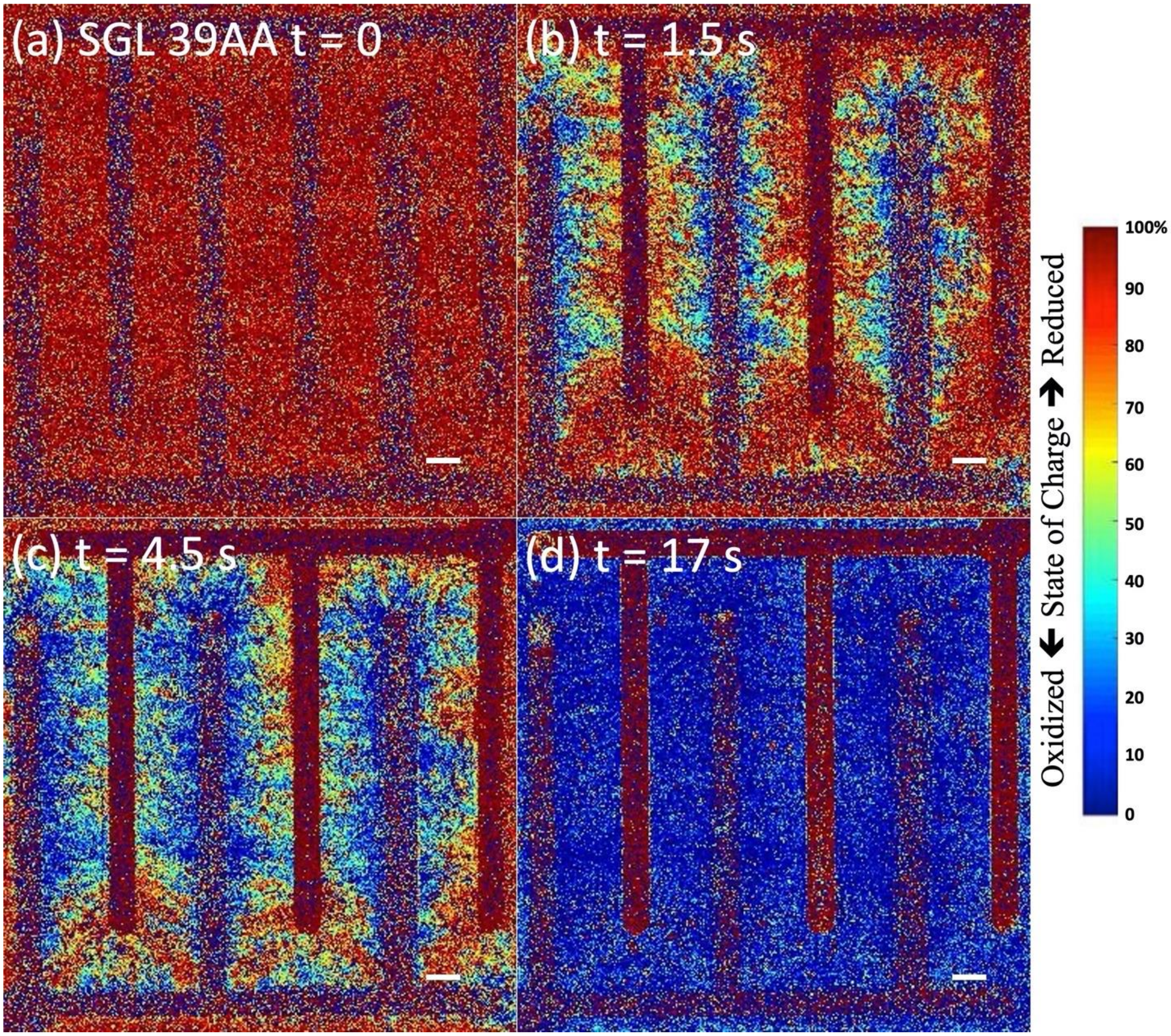

Figure S4. **Time evolution of electrolyte advection-diffusion across the entire flow field area.** Fluorescence microscope images of the IDFF on top of SGL 10AA carbon paper. (a) Fully reduced H_2AQDS brightens the electrode area under the land. (b) and (c) Oxidized AQDS is introduced at 100 mL/h, displacing the reduced electrolyte. Heterogeneous flow distribution remains evident at this scale. (d) Fully oxidized AQDS has completely refreshed the electrode. Outlet channels remain red due to the lingering reduced H_2AQDS. All scale bars are 1mm.

Note S3

Figure S4Figure S4 captures the full 2 cm^2 IDFF over an SGL 10AA carbon paper. This shows that fluorescence microscopy can be used as a valuable *in situ* technique with the capability of spanning multiple length scales from the microstructure to the macrostructure. Figure S4(a) and (d) show the electrode with fully reduced H_2AQDS, and fully oxidized AQDS respectively. In Figure S4(d) the channels are brighter from previously reduced H_2AQDS. Figure S4(b) and (c) show the transition period as AQDS is pumped into the cell, replacing H_2AQDS. Even at this macro-scale, the flow heterogeneity between the inlet and outlet channels is clearly visible and stagnation effects near the ends of the channels are evident.

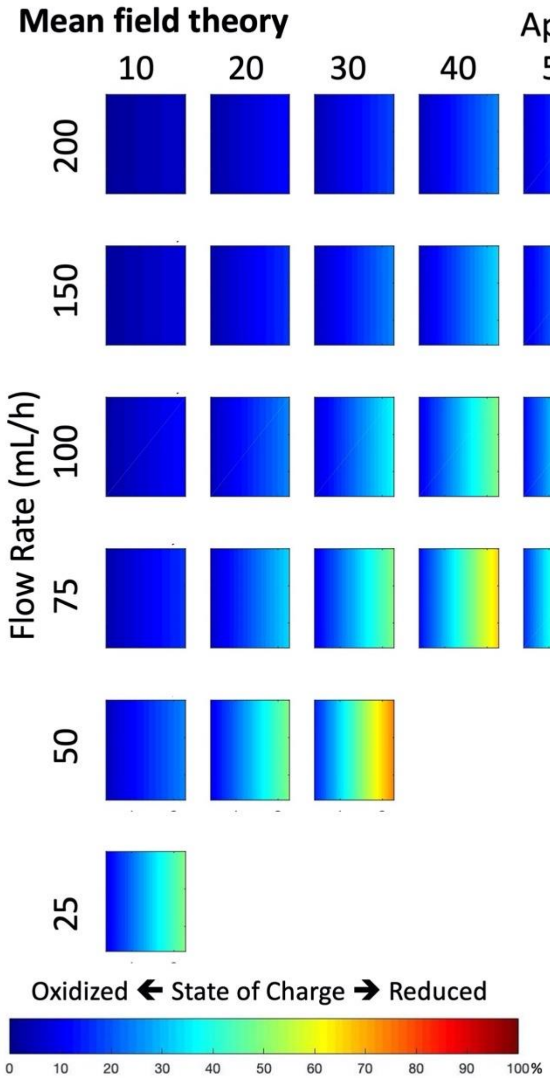

Figure S5. **Mean field theory 1D model for reaction-flow across a middle land**. Each row terminates when the applied current would exceed 100% utilization assuming a 10 mM, 2-electron reduction electrolyte. Unlike the experimental maps, this figure does not include a potentiostatic hold.

Note S4

To compare the experimental fluorescence-flow-current profiles, the MFT is applied to a simulated electrode assuming the same range of flow rates and applied currents as the experiments. Figure S5 details those idealized reaction-flow maps ending each row by displaying the maximum reactant utilization profile before the theoretical utilization exceeds 1.0. The 200-mL/h flow rate row is truncated for space constraints. The MFT used here assumes no mass transport overpotential and no limiting current.

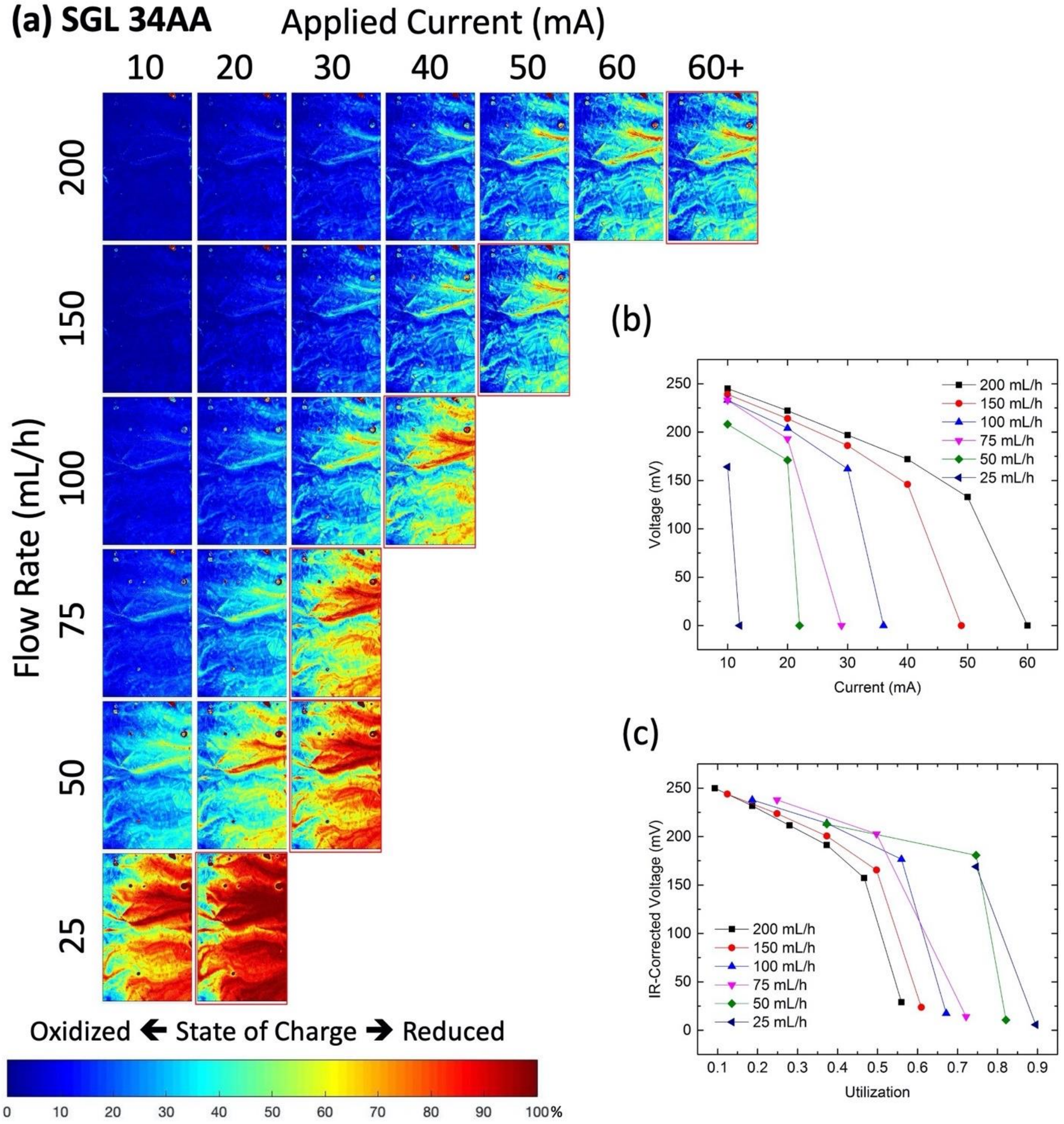

Figure S6. **Flow profiles with coupled steady state advection and constant current reduction through SGL 34AA electrode**. (a) Steady state fluorescence maps of 10 mM AQDS through SGL 34AA along a middle land, varying the electrolyte volumetric flow rate and applied current. The last figure in each row, indicated by a red border, is measured potentiostatically at 0 mV rather than galvanostatically. (b) Voltage vs current polarization plot corresponding to the steady state condition for each image. (c) IR-Corrected voltage (subtracted high frequency resistance) as a function of utilization assuming 10 mM, 2-electron reduction AQDS solution.

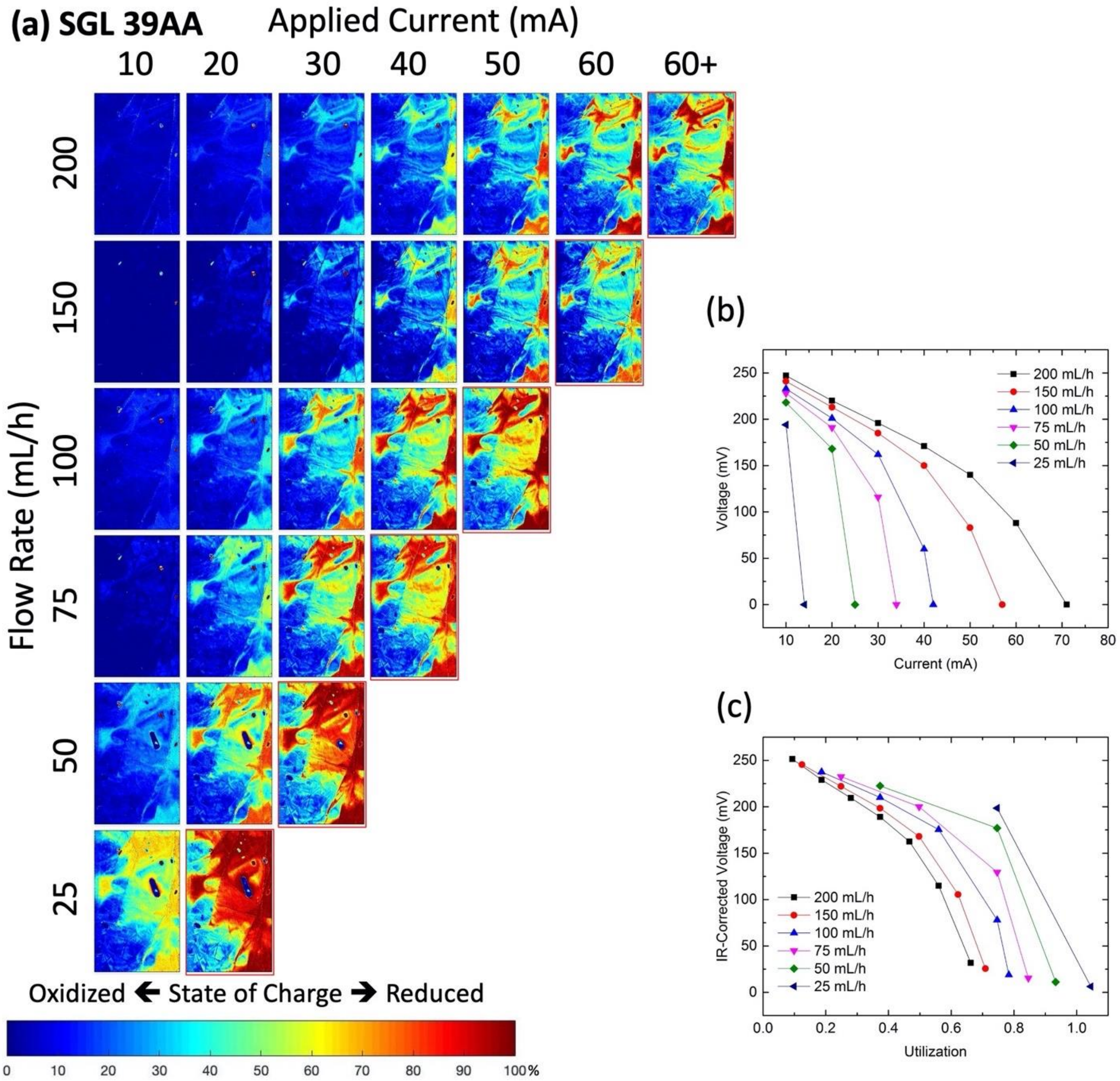

Figure S7. **Flow profiles with coupled steady state advection and constant current reduction through SGL 39AA electrode**. (a) Steady state fluorescence maps of 10 mM AQDS through SGL 39AA along a middle land, varying the electrolyte volumetric flow rate and applied current. The last figure in each row, indicated by a red border, is measured potentiostatically at 0 mV rather than galvanostatically. (b) Voltage vs current polarization plot corresponding to the steady state condition for each image. (c) IR-Corrected voltage (subtracted high frequency resistance) as a function of utilization assuming 10 mM, 2-electron reduction AQDS solution. Points greater than Utilization = 1 suggest that the electrolyte concentration is likely closer to 12 mM.

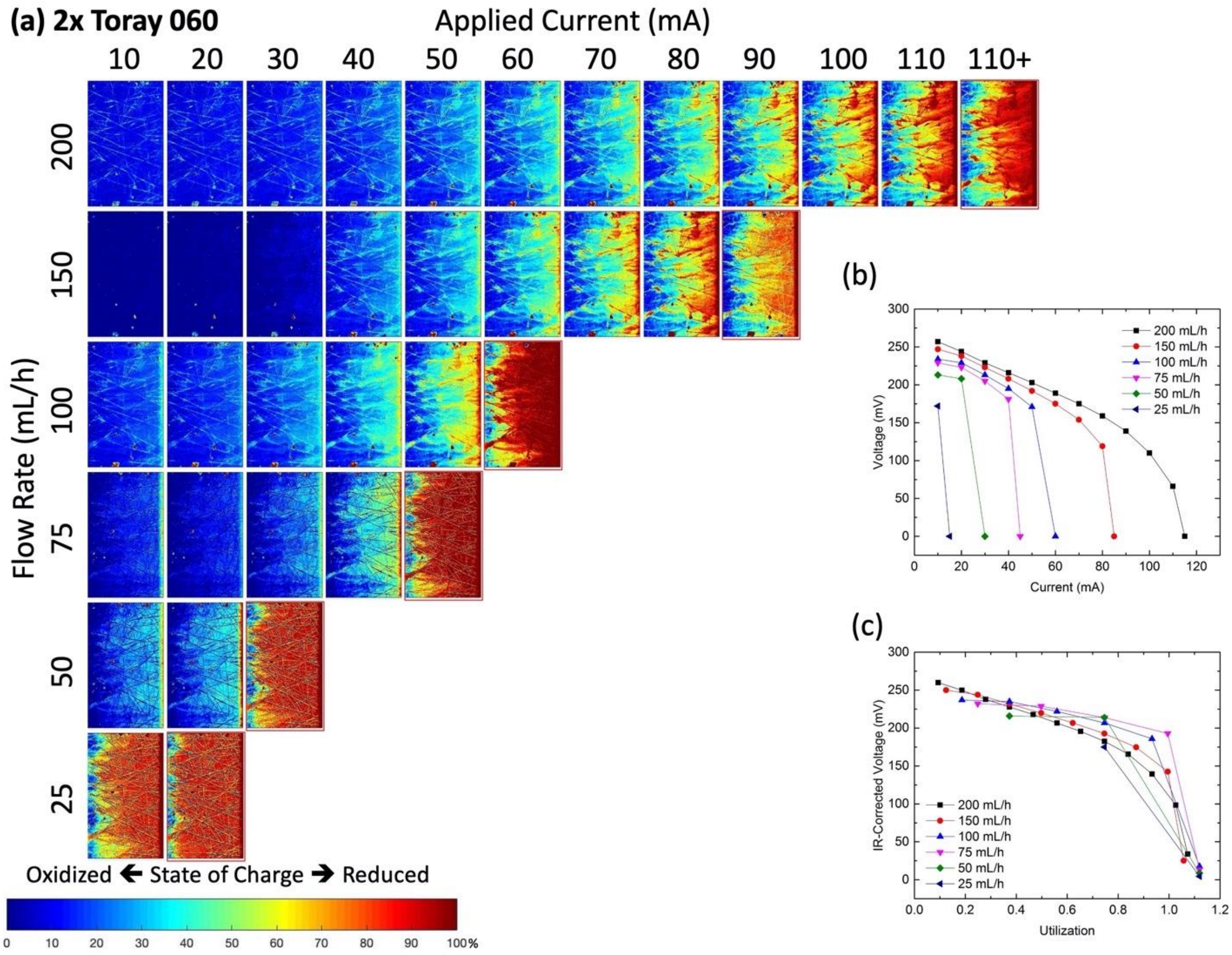

Figure S8. **Flow profiles with coupled steady state advection and constant current reduction through 2x Toray 060 electrode**. (a) Steady state fluorescence maps of 10 mM AQDS through 2x Toray 060 along a middle land, varying the electrolyte volumetric flow rate and applied current. The last figure in each row, indicated by a red border, is measured potentiostatically at 0 mV rather than galvanostatically. (b) Voltage vs current polarization plot corresponding to the steady state condition for each image. (c) IR-Corrected voltage (subtracted high frequency resistance) as a function of utilization assuming 10 mM, 2-electron reduction AQDS solution. Points greater than Utilization = 1 suggest that the electrolyte concentration is likely closer to 12 mM.

Note S5

Figure S6, Figure S7, and Figure S8 depict similar steady state fluorescence maps to Figure 5 in the main text. Though SGL 34AA has similar ohmic resistance to the other electrodes as seen by the initial slope in the high-flow results displayed in Figure S6(b), the electrode has a very early onset mass transport overpotential. This is most clearly seen in Figure S6(c) where the utilization at high flow rates only just exceeds 0.55. The absence of a highly-reduced region in the fluorescence maps at higher flow rates and current densities also appears to correlate to high mass transport overpotentials. For example, the 2x Toray 060 featured in Figure S8 is able to access very high electronic currents and therefore utilizations. The prominent transition from fully oxidized (blue) to fully reduced (red) at the end of each row in the fluorescence images indicates exceptionally high electrolyte utilizations. This is also reflected in Figure S8(c) where nominally the same utilization is accessed across the range of flow rates. Here again we note the ability to access a utilization > 1 is likely due to slight deviations in true electrolyte concentration.

From these maps, we can strengthen the hypothesis that a greater homogeneity in the electrolyte fluid flow profile within a redox flow battery has the potential to improve the full cell performance. We observe from the fluorescence maps that the 2x Toray 060 most closely resembles the MFT map in Figure S5. The Toray 060 experiment closely mirrors the maximum attainable current densities across the range of flow rates probed here when compared to the MFT approximations before exceeding a utilization of 1. Given the similarities in the morphology detailed by SEM in Figure S1. , it is not clear if and how particular structural features of the electrode lead to enhanced mass transport properties.

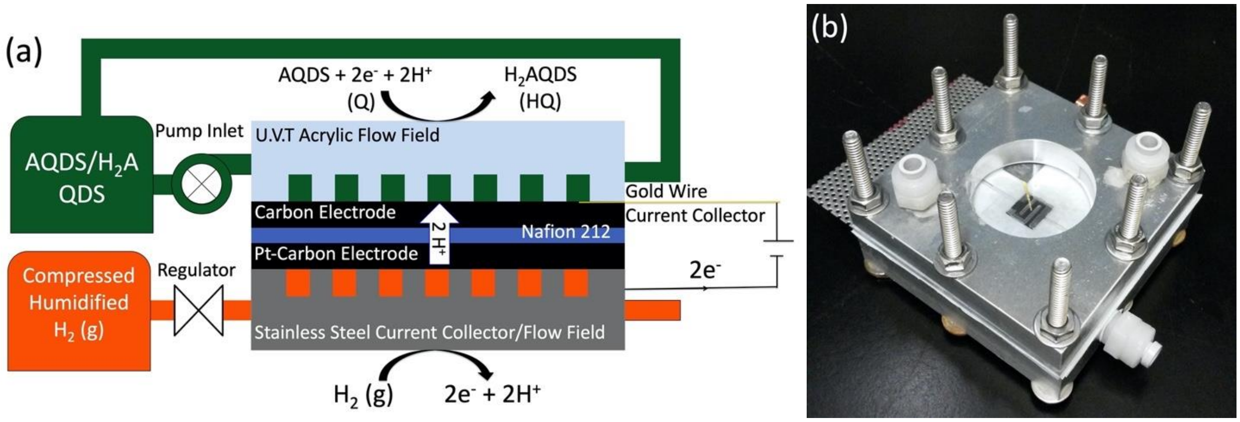

Figure S9. **Schematic and image of the fluorescence cell assembly.** (a) Schematic and materials for the quinone-hydrogen flow cell (QHFC) used throughout this work. The posolyte reservoir starts at 100% AQDS for all experiments. (b) Photograph of assembled QHFC with a UV-transparent viewing window to enable bright field and fluorescence microscopy.

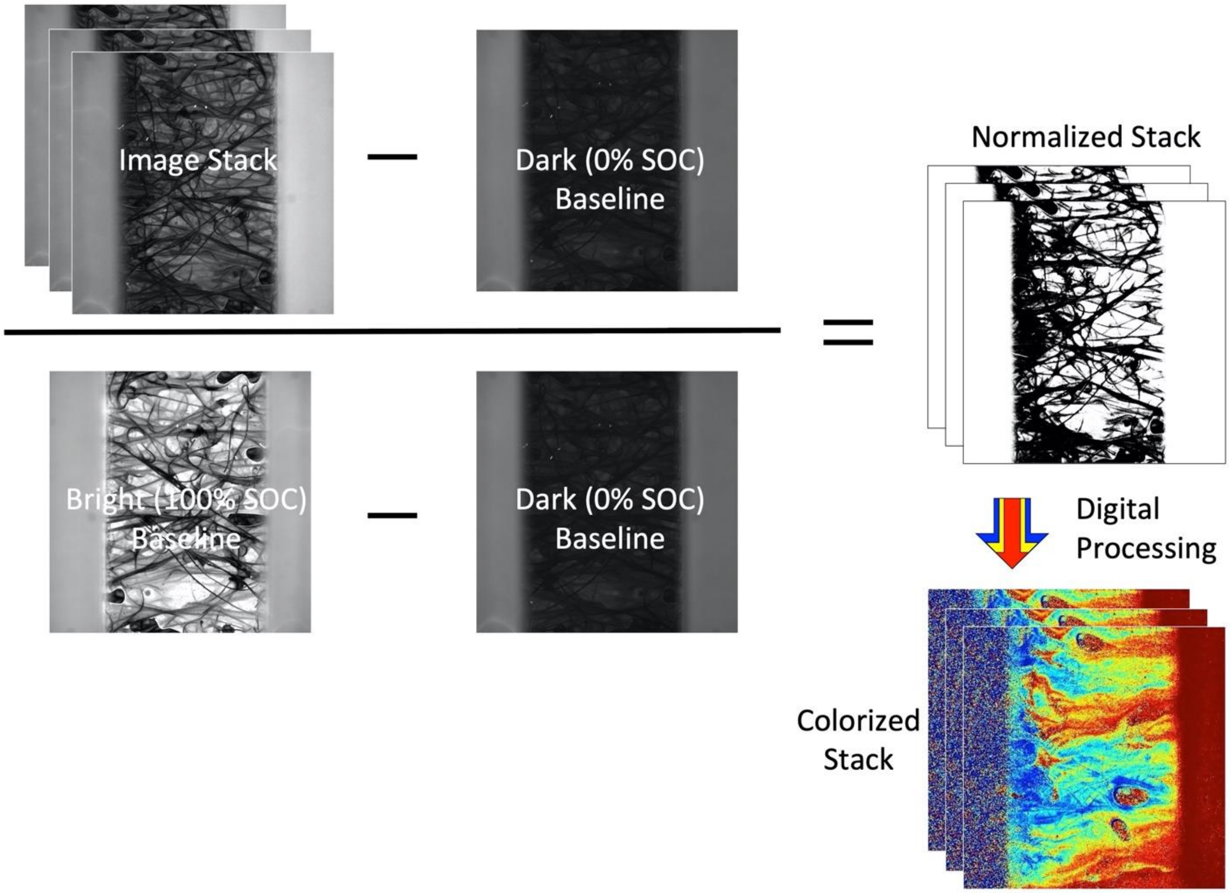

Figure S10. **Fluorescence image processing procedure**. Prior to performing an experimental series, a dark (0% SOC) baseline series is measured while holding the potential at +600 mV, oxidizing any remaining H_2AQDS to AQDS. A bright (100% SOC) baseline is also taken after holding a non-flowing electrolyte at 0 mV for 60 seconds or when the reducing current reaches a steady state. Image frames from experiments at the same location as the baselines are normalized between 0% and 100% SOC by subtracting the dark baseline, and dividing by the difference between the bright and dark baselines, creating a normalized image stack with grey scale between 0 and 1. These are then translated from grey scale to a color map.

Note S6

The image processing procedure for all of these experiments is outlined in Figure S10. All colorized images have been normalized using this procedure and use the "Jet" color scheme. Blue indicates oxidized AQDS (0% SOC) and red indicates reduced H_2AQDS (100% SOC).

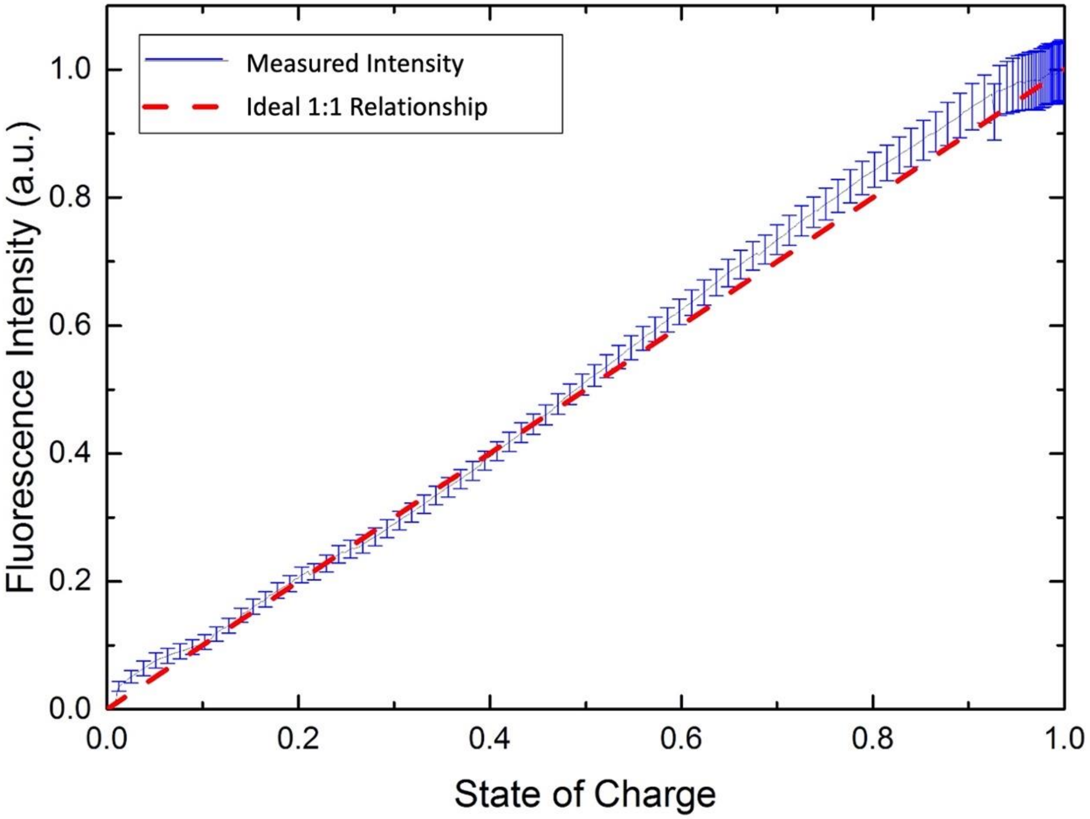

Figure S11. **Calibrated fluorescence intensity as a function of electrolyte state of charge (SOC) for 10 mM AQDS in 1 M H_2SO_4.** Error bars indicate the standard deviation in intensity at measured SOCs. The linear, 1:1 relationship between the minimum and maximum fluorescence intensity and the SOC enables the image processing procedure described in Figure S10. We note that this relationship may not hold at higher concentrations due to the optical attenuation of the AQDS oxidized quinone, reduced hydroquinone, or the quinhydrone dimer[2].

Supplemental References:

[1] Kumar, S. K., Jayanti, S. (2017). Effect of electrode intrusion on pressure drop and electrochemical performance of an all-vanadium redox flow battery. Journal of Power Sources 360, 548-558.

[2] Tong, L., Chen, Q., Wong, A. A., Gómez-Bombarelli, R., Aspuru-Guzik, A., Gordon, R. G., Aziz, M. J. (2017). UV-Vis spectrophotometry of quinone flow battery electrolyte for in situ monitoring and improved electrochemical modeling of potential and quinhydrone formation. Physical Chemistry Chemical Physics 19, 31684-31691.